Flow Control in a Cascade Thrust Reverser

A. N. Gissen[1], B. Vukasinovic[1], N. O. Packard[2], D. P. Brzozowski[3], and A. Glezer[1]

[1]*Woodruff School of Mechanical Engineering, Georgia Institute of Technology, Atlanta, GA 30332-0405.*

[2]*The Boeing Company, Seattle, WA, 98124.*

[3]*The Boeing Company, St. Louis, MO, 63166.*

Abstract

The present experimental investigation explores utilization of active flow control for mitigation of the flow separation over a shortened turning section of a cascade thrust reverser, also known as a bullnose. Such reduction in nominal thrust reverser length, with minimal or no penalty in increased drag and reduced reversed thrust, would reduce both wetted area and weight of the nacelle. In order to minimize the performance penalty, the shortened thrust reverser sector model is equipped with an array of small-scale fluidic oscillating jets that are utilized as the flow control elements for the oncoming Mach numbers $M \approx 0.24 - 0.53$. The flow control effectiveness is demonstrated over four bullnose geometries, down to 47% of the nominal bullnose length. The established scaling laws indicate that the mass flow rate recovery is directly proportional to the actuation flow rate for a given flow configuration and condition, and strongly nonlinear with the flow pressure ratio for a given flow control rate. Furthermore, it is shown that, in terms of the dimensionless flow control parameter C_q, low- and high-curvature bullnose geometries exhibit different trends in the thrust reverser mass flow rate recovery.

1. Background

Thrust reversers are integrated in aircraft jet engines with the objective of exploiting engine thrust to rapidly decelerate the aircraft for controlled, stable landings, especially in bad weather conditions when the runway can be wet or icy, and reducing reliance and wear on wheel brakes (Yetter, 1995). Thrust reversers operate by directing part or the entire engine thrust forward using mechanical deflectors that are inserted in the stream of the exhaust jet. While there are a number of designs for thrust reversers, this work focuses on cascade type thrust reversers. For the aerodynamics associated with other designs, see a detailed study by Poland (1967).

A schematic of a typical cascade type thrust reverser in the deployed configuration is shown in Figure 1 (after Butterfield et al., 2006). Air entering the diffuser (A) is split such that a percentage of the air is ingested into the engine and is used for combustion and the rest bypasses the engine and is accelerated by a large fan (not shown). This bypass air then exits through a nozzle (B) and generates a significant portion of the overall thrust in turbofan engines under normal operating conditions. During deployment of a thrust reverser, this bypass air is caused to exit (C) at an orientation that generates thrust in the reverse direction generated by the engine under normal operation. In order to efficiently direct air to the exit as shown (C), a series of operations take place. To begin with, a portion of the cowl (D) moves aft. This causes a blocker door to be deployed (E) which is designed to prevent the flow from exiting through the exit nozzle (B). In cascade type thrust reversers, the aft motion of the cowl (D) also exposes an array, or a cascade of turning vanes, which the flow is forced to exit through. These turning vanes can be adjusted to generate various exit airflow vectoring. A cascade type thrust reverser installed on a turbojet powered fighter plane in a study by Kohl and Algranti (1957) demonstrated decreased stopping distances and reduced weight compared to the, then, standard design which did not include a cascade of turning vanes.

The design considerations for a cascade type thrust reverser related to the present study can be found in a publication by Wood and McCoy (1969). They describe the deployment, stowage and nacelle movement

typical in a thrust reverser and, briefly, describe some of the advantages of this design. The interaction of the reversing flow with the wing, ground, and body of the aircraft can often generate unexpected and dangerous situations, such as unpredictable variations in thrust magnitude and orientation. A study addressing the issues of the interaction of the flow exiting the reversers with other aircraft components and the ground by Hegen and Kooi (2005) presents a very thorough investigation of two different types of thrust reversers integrated into a scaled model airframe. Other dangerous situations can arise when the orientation of the thrust reverser exhaust can be such that re-ingestion of the exhaust flow is possible. This situation can result in severe engine surge and stall. A study performed by Dietrich and Gutierrez (1976) investigated the performance effects of airframe thrust reverser interaction with special focus on re-ingestion. Another example of re-ingestion was found on the C-17 where redesign of the thrust reverser assembly was necessary following several severe engine stall events (Johns, 2000).

Flow control efforts to improve the performance of thrust reversers have been the subject of a number of studies. A NASA report by Arbiter (1985) examines the effects of rounding and rotating the surface over which the flow is turned (the bullnose, G in Figure 1). The flow through the duct was improved, but at the expense of very high rotation speeds. A patent by Smith (1977) details how a coanda jet installation in a cascadeless thrust reverser, where the coanda jet is applied to the outside of the bullnose, might be used to improve the performance of the duct. More recently a study by Hall et al. (2006) demonstrated how flow control in the form of steady coanda jets applied to several locations within a natural blockage cascadeless thrust reverser can be used to improve the flow turning and overall generated thrust.

The large forces imparted on thrust reverser assemblies dictate the use of heavy components. One strategy for reducing the weight penalty associated with the installation of a thrust reverser involves the reduction in the overall length of the thrust reverser assembly. This strategy has two primary advantages. First, a reduction in the length of the thrust reverser would reduce the weight associated with the heavy components which constitute the thrust reverser assembly. Second, a reduction in the thrust reverser length would reduce the length of the nacelle. This reduction in length of the nacelle would reduce the wetted area of the nacelle thereby reducing the aircraft drag under cruise conditions.

The reason that such modifications have not been made to thrust reverser designs involves the efficiency with which the flow exits the thrust reverser. A shorter thrust reverser would necessitate a decrease in the radius of curvature over which the flow turns. This component, often referred to as the ‘bullnose’, is shown in Figure 1 (G). Reduction in the bullnose length results in separation over the bullnose surface which generates losses. This, in turn, results in a reduction of the magnitude of the reverse thrust generated through a reduction in the mass flow rate through the duct due to increased drag. In addition, an increase in pressure drop across the thrust reverser assembly would place larger, and potentially damaging, load on the main engine fan.

For these reasons, it is the primary goal of the current work to explore utilization of an active flow control strategy to reduce the separation region over the bullnose, generated by a reduction in its length. Suppression of the flow separation would lead to a reduction of the flow losses and to an increase in the mass flow rate through the thrust reverser assembly, which, in turn, would generate more reverse thrust. Hence, primary focus of the current work is demonstration of the feasibility of mitigation of the adverse effects associated with length reductions in thrust reverser assemblies by the active flow control, while assessing its unique flow topology as well.

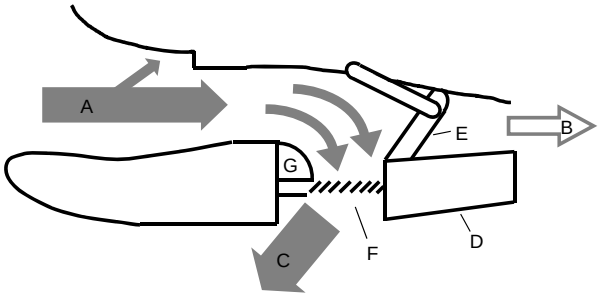

Figure 1. *Schematics of a typical cascade type thrust reverser (Butterfield et al., 2006).*

2. Experimental Setup

A thrust reverser model geometry that is designed for the present experiments is shown schematically in Figures 2a and b. This configuration mimics the thrust reverser with the blocker door fully deployed and the jet flow (from left to right) forced to turn at a nominal angle of 45° and exit through the cascade vanes (at the bottom) that assist in vectoring the flow. The upstream jet flow turns around a 'bullnose' corner at the bottom wall. The bullnose is of nominal height H = 17 mm, a parameter which is used as a characteristic length of the geometry. Owing to the strong turn, the flow typically separates at this surface thus significantly diminishing the effectiveness of the cascade vanes immediately downstream, and increasing drag. The tested thrust reverser section has an annular geometry, having a sector angle of 55° and throat outer radius of 8.2H. The radial height of the test section at the apex of the bullnose (x = 0) is 4.2H. The cascades span an axial distance of 5.1H. The facility is driven by a 66.3 bhp blower that can deliver Q = 3,907 m^3/hr flow rate at 26.3 kPa. The thrust reverser section is mounted in a high-speed open-return axisymmetric duct facility with a diameter of 11.5H. The thrust reverser duct is attached to this circular outlet section of the duct facility using an adapter section, filled with honeycomb and a mesh screen, in an effort to provide uniform flow to the thrust reverser section.

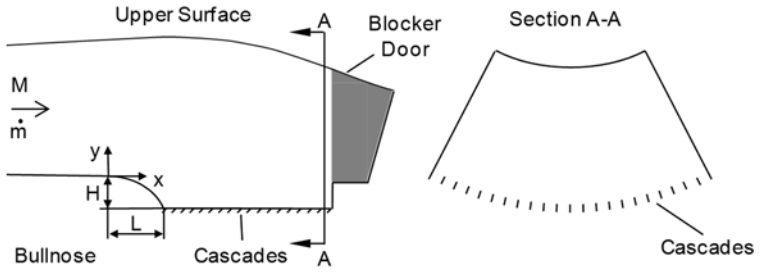

Figure 2. *Schematics of the thrust reverser test section: a) side view of the duct and b) an upstream view of the annular sector cross section.*

As a flow diagnostics component, particle image velocimetry (PIV) utilizes a glass insert installed in the upper surface, through which a laser sheet illuminates the flow over the surface of the bullnose. The PIV camera is located such that it has optical access through Plexiglas side panels.

The tested shapes of the bullnoses are described in Figure 3. The bullnoses are of decreasing length with respect to the nominal, baseline (B) bullnose, and are labeled as A1 through A4, having the length progressively shortened to 82%, 65%, 59%, and 47% of the baseline length, respectively, while preserving the bullnose height H. Similarity in shape is preserved throughout the majority of the bullnose as demonstrated by the scaling factor of $L^{0.8}$, on which this family of bullnose shapes is approximately based. This scaling of the shape indicates how the curvature and thereby the pressure gradient scale with the length of the bullnose. The main purpose of this study is to determine how the flow control can be used to alleviate the detrimental effects of reduced bullnose length. In order to accommodate these decreases in bullnose length, the blocker door (see Figure 2) and the cascades are moved in the axial (-x) direction, along with the bullnose shortening. In this manner, the cascades, and thereby the exit area of the duct, are kept constant for all the bullnoses tested.

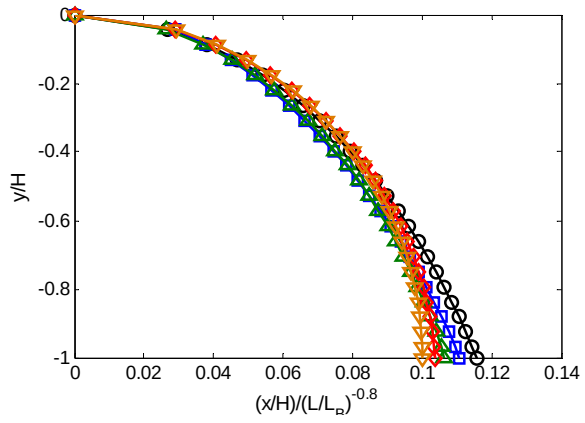

Figure 3. *Scaled profiles of the baseline bulllnose B and aggressive bullnoses A1 – A4, where L/H = 1.7 (○), 1.4 (□), 1.1(Δ), 1.0 (◊), 0.8 (▽), for the bullnoses B, A1, A2, A3 and A4, respectively.*

The flow control deployed in this study utilizes fluidic oscillating jets, which have no moving parts and are easier to integrate within the confined space of the thrust reverser model. In addition, a clear advantage of fluidic oscillator jets for propulsion airborne applications is that the actuation fluid can be easily diverted from the engine's compressor and returned to the duct flow without reducing the overall mass flow rate. These jets are deployed in the present model at a constant x/H across the span of the bullnose in an array of 21 jets, where the x/H location is

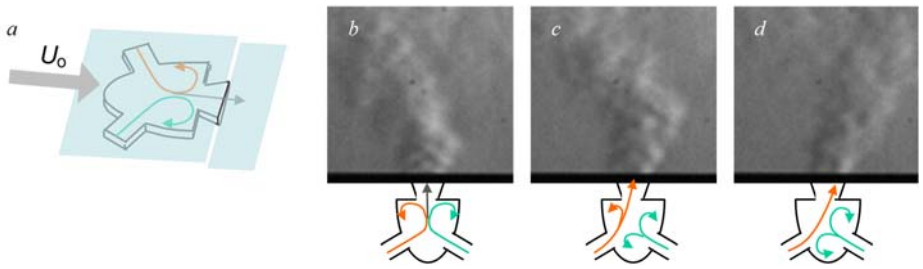

Figure 4. *Schematics illustrating integration into the bullnose surface (a) and schlieren visualization (b–d) of the oscillating jet past the actuator orifice. Bottom schematics illustrates unstable interaction of the two fluid streams within the actuator body.*

determined by a study of the flow separation (cf. Figures 7 and 8). The jets are integrated and faired into the surface, where each jet orifice is 1.5 × 1.5 mm on the sides and neighboring jets are spaced 7.5 mm apart. The flow control jets oscillate in the spanwise direction and issue nominally tangentially to the bullnose's moldline. The jet oscillating frequency is a weak function of the fluidic oscillator flow rate and, for a typical flow rates utilized in the current test, the frequency is approximately 10 kHz, as measured by a hotwire anemometer. The present control approach of separated flows is to decouple the actuation frequency from the unstable frequencies of the separating shear layer using 'high frequency' actuation which couples directly to the small-scale motions within the flow. It was shown in a planar shear layer that when the actuation frequency is higher than about twice the highest 'natural' frequency of the separating flow, the unstable frequencies of the 'natural' shear layer are suppressed (Vukasinovic, Rusak, and Glezer, 2010). The highest natural frequency in a free shear layer can be estimated from the characteristic Strouhal number $St_\theta = f_c \cdot \theta_o / U_c \approx 0.022$ (e.g., Ho and Huerre, 1984), where θ_o is the momentum thickness of the boundary layer at separation. In the present experiments the boundary layer momentum thickness is estimated to be about 1 mm yielding $f_c \approx 4$ kHz at $M = 0.5$. Therefore, the actuation frequency in the present work is selected to be about 10 kHz. The flow control parameter is defined as the mass flow rate coefficient C_q, which is the ratio between the total mass flow rate through the jet array and the mass flow rate through the test section.

Schematics showing how the control jet is embedded in the surface is shown in Figure 4a. The fluidic actuator is integrated under the bullnose moldline such that its orifice issues the jet as close to tangential to the local bullnose surface, which is also assisted by a slight overhang above the jet orifice. A single fluidic oscillating jet is also characterized on the bench, and its operation is illustrated in Figures 4b-d, which show schlieren visualization of the resulting jet, issuing in still air. Along with each instance of the jet oscillation captured in schlieren images, schematics underneath the images shows relevant internal interactions of the two supply streams to the fluidic oscillator, which give rise to the issued jet oscillations. The fluidic oscillating jet cavity has two entrances which cause two air jets to interact in an unstable fashion. Figure 4b shows the primary exit jet emanating from the exit nominally vertically as the two jets are instantaneously balanced against each other. The exit of the fluidic oscillating cavity acts as a coanda surface. This, combined with the unstable interaction of the jets inside the cavity, causes the primary exit jet to 'stick' to one side of the exit orifice, as is seen in the vectoring of jet in the schlieren image of Figure 4c. As the vortex pair formed by the right hand jet (shown in green in Figure 4c) takes up more and more of the cavity (Figure 4d), the exit jet is vectored further to the right as shown in Figure 4d. This situation is unstable and the next step (not shown) results in the right hand vortex (shown in green)

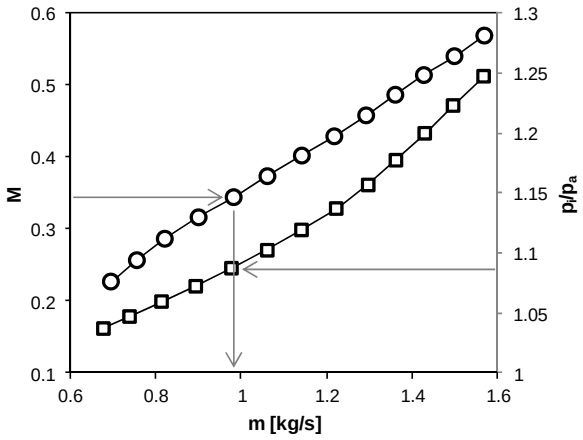

Figure 5. *Variation of the mass flow rate through the thrust reverser with Mach number and the pressure ratio for the baseline flow over a nominal B bullnose (L/H = 1.7).*

forcing the left hand jet to circulate and the right hand jet to dominate the exit flow causing the same process to occur but with the opposite symmetry. For reference, the exit orifice of the jet is 1.5 mm across. The height of the jets defines the height of the overhang within which the array of jets is housed. For a more detailed description of the physical mechanisms behind the operation of the fluidic oscillating/sweeping jets, see an overview by Raghu (2013) and Gregory and Tomac (2013).

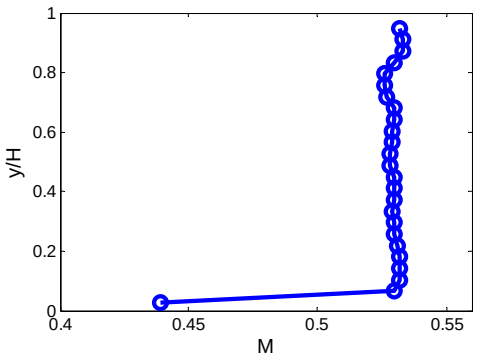

Figure 6. *Cross stream variation of the Mach number measured at the inlet of the thrust reverser tests section (x/H = -6.56) at p_i/p_a = 1.24.*

Pressure measurements along the surface of the bullnose are performed using an Esterline 98RK-1 pressure scanner with 9816 (34.47kPa) modules. Each static pressure measurement is an average of 125,000 samples. The accuracy of the D200 sensors in the 9816 module is within 52 Pa (0.1% of full scale). Besides the surface static pressure measurements, additional time-invariant pressure measurements of the Pitot probe are utilized to characterize the oncoming Mach number of the flow into the thrust reverser sector, where the Pitot probe is located at the entrance of the test section at a distance of 6.5*H*, upstream (-*x* direction) from the apex of the bullnose. The flow condition is defined through the pressure ratio between the total pressure measured by the Pitot probe and the pressure that the facility vents to, i.e., the atmospheric pressure. This pressure ratio can be adjusted by the computer-controlled blower motor of the wind tunnel facility, and it is varied between p_i/p_a = 1.04 – 1.25 in the present investigation, which corresponds to the oncoming duct Mach numbers $M \approx 0.24 - 0.53$ for the baseline B bullnose.

Temperature in the facility is controlled via a sealed heat exchanger, connected to the lab chilled water supply. The flow rate of the chilled water supplied to the heat exchanger is controlled via a thermocouple-driven controller attached to a three-way bypass valve in the chiller water supply line. The control thermocouple is placed in the exit plume of the facility. Thermocouples are also placed on either side of the heat exchanger and at the inlet of the wind tunnel. Temperatures are controlled to a repeatability of 1 degree F.

The 'baseline' bullnose geometry represents the current shape of bullnoses used in conventional thrust reversers (Figure 1). The variation of the time-averaged mass flow rate ($\dot{m}$) through the thrust reverser duct with the inlet Mach number and the pressure ratio p_i/p_a are shown in Figure 5. These data show a nearly linear dependence of $\dot{m}$ on *M*, and that $\dot{m} \sim (p_i/p_a)^{2/5}$. Mass flow rate through the test section is a function of the pressure ratio across the test section, but increasing mass flow rate also increases the losses, which induce nonlinear dependence at higher flow rates in the complex geometry duct with flow separation. The uniformity of the inlet flow to the test section was assessed from a cross-stream distribution of the Mach number (p_i/p_a = 1.24) in the y-direction (Figure 6) that was measured by traversing a Pitot-static tube normal to the surface at the midspan. The cross stream height of the section at this inlet station is 3.8*H*. The present measurements indicate that the thickness of the wall boundary layer is smaller than 3 mm which is commensurate with the presence of a contraction upstream of the thrust reverser duct and its adapter section. The data in Figure 6 indicate that the inlet flow is nominally-uniform in the y-ordinate direction at the pressure ratio of p_i/p_a = 1.24.

3. Characterization of the Baseline Flow over the Bullnose Section

The goal of the present investigations is to assess the degree to which the bullnose, shorter than the nominal one, affects losses in the thrust reverser section, and to what extent active separation control can be employed to restore the similar level of reversed thrust by delaying or suppressing the internal flow separation. In addition to the nominal bullnose geometry (referred to as B), four shorter bullnose configurations (labeled A1-A4 where A4 has the most aggressive reduction in length) are built and tested. The shorter configurations are created by reducing the radius of the bullnose surface relative to the baseline (B) geometry as already shown in Figure 3.

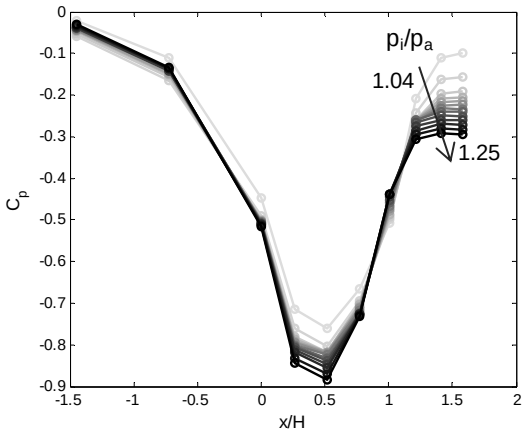

Figure 7. *Static pressure distribution along the centerline of the baseline bullnose (L/H = 1.7) over a range of pressure ratios 1.04 < p_i/p_a < 1.25.*

Static pressure profiles on the surface of the bullnose, measured along the centerline of the baseline (B) bullnose for a range of pressure ratios $1.04 < p_i/p_a < 1.25$ are shown in Figure 7 in terms of the pressure coefficient $C_p = \frac{2}{\gamma M_r^2}\left(\frac{p}{p_r} - 1\right)$, where the reference Mach number and static pressure are measured at the thrust reverser face plane. The measurements are taken along the surface described in Figure 3. Due to the shape of the outer surface of the duct, the flow is accelerating before it reaches the apex of the bullnose ($x/H = 0$). As the flow accelerates along the curved surface, the pressure reaches its minimum value at about $x/H = 0.5$. The adverse pressure gradient associated with the expansion over the remaining curved surface causes the fluid to decelerate, as indicated by an increase in the static pressure measured on the surface. This adverse pressure gradient continues to slow the flow until, at approximately $x/H = 1.2$, the flow separates. This separation is indicated by a decrease in the pressure gradient measured along the surface, due to the fact that the pressure gradient on the surface is dominated by the bulk flow pressure in the separated region. As the pressure ratio (p_i/p_a) and the flow speed increase, the minimum pressure decreases, but the location of the minimum pressure stays at nominally the same location. In contrast, the separation point moves further upstream for increasing pressure ratio across the test section, as indicated by the flattening of the pressure gradient observed over the three most downstream pressure ports. Therefore, it can be argued that flow separation off the bullnose is primarily driven by the adverse pressure gradient that is imposed by the aggressive curvature and the downstream flow sections in this subsonic internal flow. The large stagnation region that develops over the blocker door has a tremendous effect on

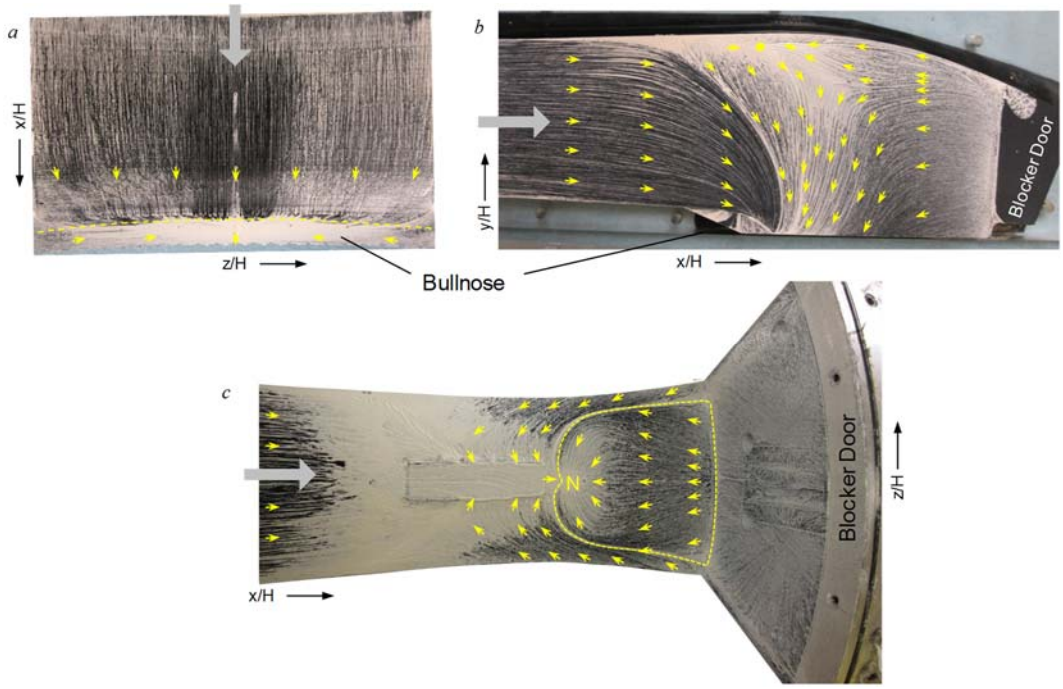

Figure 8. *Surface oil visualization of the base flow (p_i/p_a = 1.25) along the bullnose (a), side (b), and top (c) surfaces of the thrust reverser.*

and couples to the separation dynamics, amplifying the unsteadiness of the impinging flow. In realistic installations, the separation unsteadiness can also be affected by global upstream and downstream unsteadiness of the bulk flow.

Complexity and strong three-dimensionality of the flow within a thrust reverser sector is illustrated in Figure 8 using the surface oil-flow visualization, for the base flow at $p_i/p_a = 1.25$. To assist in analysis of the base flow topology, local directions of the flow are marked with overlaid arrows. The visualization over the bullnose (Figure 8a) shows the flow separation over the diverging bullnose surface, as is evident by a build-up of oil along the separation line, which is marked by a dashed line in the figure. This oil buildup indicates that separation along the centerline occurs at $x/H = 1$. This is slightly upstream from where the change in slope of the pressure trace shown in Figure 7 suggests incipient separation. The slight curve in the separation line indicates that separation is a weak function of the distance from the centerline of the facility owing to the effects of the sidewalls, which causes the curvature to increase with distance away from the centerline. More insight into the three-dimensional flow topology can be gained by analysis of the surface oil-flow visualization along the side and top surfaces of the duct, as shown in Figures 8b and c, respectively. Side wall traces (Figure 8b) indicate that most of the flow directed downward through the cascades near the side wall results from the reversed flow that is splashed from the impingement zone at the blocker door. This reversed flow collides with the oncoming flow through the duct, creating a stagnation point, marked by a dot, close to the upper surface. The oncoming flow is thereby sharply deflected towards the bullnose, having a clear demarcation line with the flow that interacts with the reversed flow. Surface flow visualization over the top surface (Figure 8c) shows that the main flow that gets diverted over the upper surface, after impingement on the blocker door, cannot simply collide with the oncoming flow near the top surface. Instead, it converges towards the separation node point (marked by *N*), lifts off the surface and creates recirculating bubble. The resulting separation region is bound by dashed contour, and it is interesting to note that it does not extend all the way to the side walls. This large separation region in the area where the blocker door and the upper surface intersect generates losses, reducing the thrust reverser mass flow rate and thereby the reverse generated thrust. While outside the scope of the present work, this large separated region, which exists in the default baseline geometry, indicates that flow control designed to influence the size of this large region of separated flow would have the potential to significantly further reduce losses and increase the flow rate through the thrust reverser.

As the streamwise length of the bullnose is reduced, its radius of curvature decreases, causing the adverse streamwise pressure gradient over the surface of the bullnose to increase as shown by the distribution of static pressure along the bullnose centerline ($p_i/p_a = 1.25$, Figure 9a). As the radius of curvature near the apex of the bullnose ($x/H = 0$) decreases, the minimum pressure decreases as well. This is analogous to the

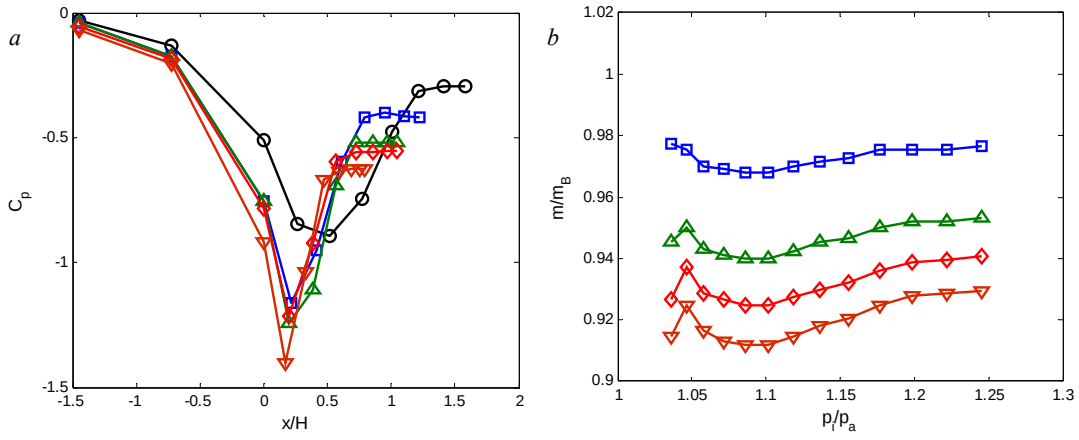

Figure 9. *Static pressure profiles along the centerline of the bullnose for $p_i/p_a = 1.25$ (a) and the variation of the relative mass flow rate through the thrust reverser with pressure ratio p_i/p_a (b) for the bullnose configurations L/H = 1.7 (○), 1.4 (□), 1.1(Δ), 1.0 (◊), and 0.8 (▽).*

leading edge of an airfoil at increasing angles of attack. For an airfoil, the suction peak increases and moves up-chord for increasing angles of attack due to the effective increase in local radius of curvature with respect to the flow. In the same way, the low pressure region caused by the radius of the bullnose increases in strength and moves upstream for decreased radius of curvature. This effect not only lowers the suction pressure over the bullnose, but also induces a decrease in pressure upstream from $x/H = 0$, as the bullnose length decreases from B to A4. The decreased radius of curvature also results in a stronger adverse pressure gradient downstream from the suction peak, which results in upstream migration of the separation point for bullnoses of decreasing radius.

4. Control of Flow Separation over the Bullnose

As shown in Section 3, the reduction in bullnose length leads to an increase in overall losses and, therefore, a decrease in mass flow rate and a loss in reverse thrust. The objective of the present investigations is to explore the utility of fluidic-based active separation control on the surface of the bullnose in order to improve the overall aerodynamic performance while using an aggressive bullnose configuration. Ideally, reduction in the thrust reverser length should be achieved at no expense in terms of its performance at the same pressure ratio. The streamwise location of the jet array (addressed in Section 2) for each bullnose configuration is determined by a separate investigation of the separation pattern using surface oil visualization and static pressure measurements, so that the jets could be placed just downstream from separation, to ensure that in the absence of actuation the presence of the array does not lead to premature separation and increased losses. The separation location in the absence of control jets is determined by the oil visualization along the centerline of the bullnose. The locations of the actuation jets (solid symbols) on the bullnose configurations are shown in Figure 10, which indicates the trends in both separation location and in locations selected for the flow control installation with the varying bullnose length L/H. As the bullnose length decreases from B-A4, the separation point in the base flow moves upstream and takes up a larger percentage of the bullnose. Bullnose A4, for example, is separated over an estimated 77% of its length, whereas the B bullnose is only separated over 40% of its length. As indicated in Figure 10, the flow control jets array is always placed downstream from the point of separation.

Although the integration of the jet array was designed to alter the surface geometry as little as possible, the presence of the array in the absence of actuation leads to some decrease in the thrust reverser mass flow rate. Figure 11a shows the variation of $\dot{m}/\dot{m}_B$ with pressure ratio for the bullnoses in the absence of the actuator array and in the presence of the inactive array (dashed and solid lines, respectively). When $\dot{m}/\dot{m}_B < 1$ for a particular pressure ratio, the mass flow rate is below that which would be attained under the same conditions for the baseline geometry without the installed actuator array. Hence, the decrement in $\dot{m}/\dot{m}_B$, seen in Figure 11a, due to the installation of the actuators is the difference between the dashed and solid lines for a given bullnose configuration. For the longest (baseline) bullnose there is a maximum reduction of the flow rate to 96.5% at $p_i/p_a = 1.03$ due to the presence of the actuator, which monotonically decreases with increasing pressure ratio and reaches 99% at $p_i/p_a = 1.2$, most likely due to the fact that incipient separation is affected by the presence of the installed jets at low pressure ratios, but becomes overtaken by the natural separation at higher pressure ratios. As the bullnoses become shorter (i.e., more aggressive, bullnoses

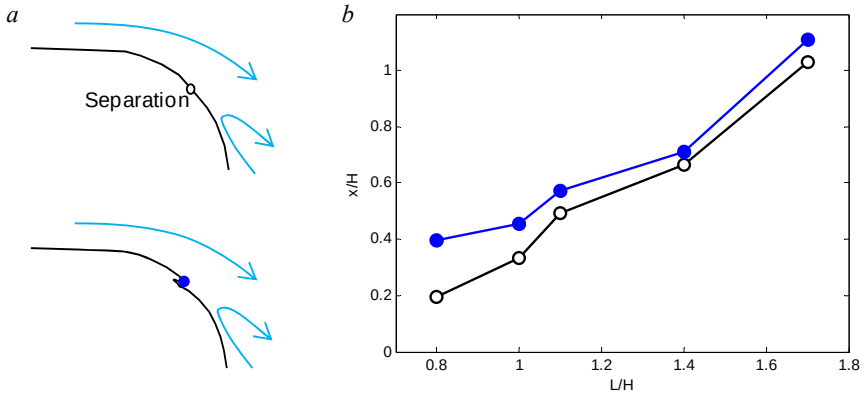

Figure 10. *Schematics of the bullnose moldline without and with the flow control array installed (a) and relative streamwise positions x/H of the flow separation (○) and the flow control integration (●), (b).*

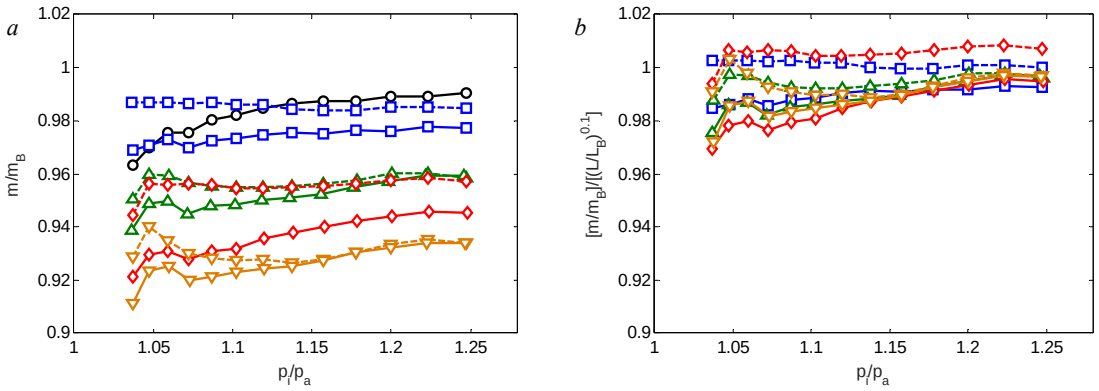

Figure 11. *Variation of the recovered mass flow rate with pressure ratio for the bullnose configurations L/H = 1.7 (○,B), 1.4 (□, A1), 1.1(Δ, A2), 1.0 (◊, A3), 0.8 (▽, A4), without (dashed) and with (solid) the flow control array installed and inactive.*

A1-A4), the losses in $\dot{m}/\dot{m}_B$ diminish with decreasing bullnose length. The outlier in this set of data, shown in Figure 11a, is the A3 geometry where the location of the actuation array is observed to be non-optimal, as the decrease in mass flow rate does not follow the trend shown in the other four bullnoses investigated. The magnitude of the decrement in mass flow rate as a result of the integration of the flow control into the surface of the bullnose is a function of the difference between the optimal location of the flow control and the actual installed location. However, unlike A3, A4 shows almost no measureable decrease in mass flow rate at the highest pressure ratios in the presence of the actuation jets. The data presented in Figure 11a indicate that the actuator configuration for A3 could be further improved (through optimized actuation placement) beyond what is inferred from the present measurements.

The geometric scaling that was described in Figure 3, is used as a guide to scale the non-dimensionalized mass flow rates plotted in Figure 11a. Scaling of the curves results in the mass flow rates being proportional to $L^{-0.1}$, with $m^* = (\dot{m}/\dot{m}_B)(L_B/L)^{0.1}$. It is interesting to note that the behavior of A1 and A3 appear to be outliers in this trend. Furthermore, when the flow control is installed but not active, the behavior over the range of pressure ratios becomes similar for all bullnose lengths due to the fact that the separation is 'triggered' by the step of the jet installation, uniformly across the bullnose, whereas in the naturally occurring separation the flow separates spanwise non-uniformly, setting up additional non-linearities in the losses generated through the duct. It is also notable that the behavior of A1 and A3 are very similar to the behavior of the baseline bullnose at low pressure ratios, as indicated in the nominally flat response at low pressure ratios in Figure 11b. In contrast, the other tested bullnoses indicate that there is a slight local maximum in relative performance at a pressure ratio of p_i/p_a = 1.06. Finally, it is pointed out that the similarity between the scaled curves indicates that, despite the complexity of this duct flow, the dominant factor that drives the reduction in mass flow rate in this study is the reduction in bullnose length.

As an introduction to the behavior of the various geometries with the flow control active, the A2 geometry is selected to represent the ability of the flow control to increase the mass flow rate through the thrust reverser. The changes effected by jet actuation on the A2 configuration are shown in Figure 12. The mass flow rate coefficient C_q, unless otherwise specified, is presented as the percentage of mass flow provided to the actuators compared to the flow through the facility at a p_i/p_a = 1.25 with the baseline (B) bullnose installed. This mass flow rate is selected as a reference and the variation of mass flow rate through the facility with pressure ratio is measured. Figure 12a demonstrates that the actuation leads to a large increase in mass flow rate through the facility over the entire range of pressure ratios tested. At low pressure ratios (p_i/p_a = 1.03), the mass flow rate is increased to 1.015, and, at higher pressure ratios (p_i/p_a = 1.24), the mass flow rate is increased from 0.95 to 0.995. This is a 4.5% improvement with approximately 1.3% mass flow rate supplied to the control jets (i.e., C_q = 0.013). Furthermore, the entire region between the curves is available to the designer simply by changing the mass flow rate to the flow control jets. It is important to note that the mass flow rate supplied to the jets is not included in the measured mass flow rate increase through the facility, as the facility mass flow rate is measured at its inlet. However, the mass flow rate

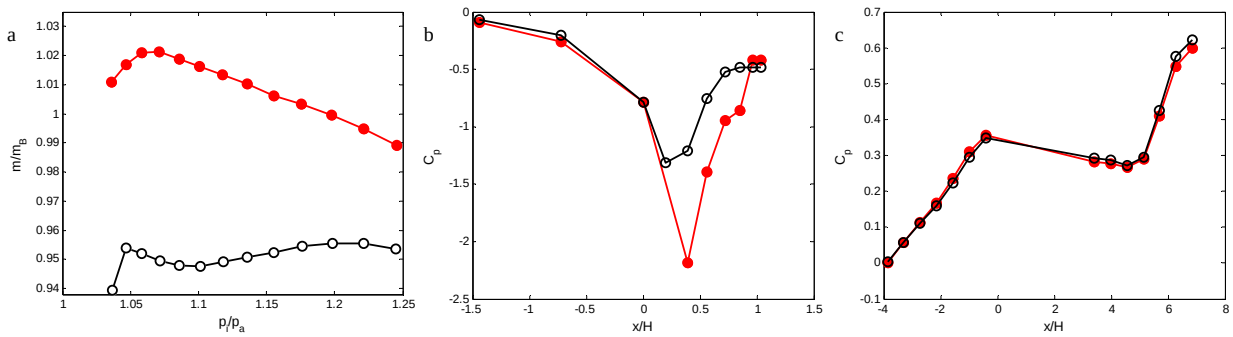

Figure 12. *Mass flow rate recovery with pressure ratio (a) and static pressure profiles along the bullnose (b) and the opposite wall (c) centerlines at p_t/p_a = 1.25, for A2 (L/H = 1.4) configuration in the absence (○) and presence of constant actuation (●) that results in C_q = 1.2% at the highest p_t/p_a.*

supplied to the jets exits the thrust reverser assembly through the vanes and provides additional reverse thrust, over and above the increases that would be induced just by the measured facility mass flow rate gain. Another observation regarding the flow control effect on the recovered flow rate through the facility seen in Figure 12a for a constant flow rate to the flow control jets is the decreased effectiveness with increased pressure ratio. This is attributed to the fixed mass flow rate through the control jets with the increased mass flow rate through the facility, which essentially lowers the jets' C_q with increased pressure ratio. Besides the decreasing C_q, it can be also argued that, as the flow separation point shifts upstream with increasing pressure ratio (c.f. Figure 7), the relative position of the jet array and the separation point cannot be optimal over all conditions tested and therefore also contributes to the falloff in the mass flow rate recovery for higher pressure ratios. In general, the plot of mass flow rate, Figure 12a, demonstrates the feasibility of using flow control to improve the performance of a shortened thrust reverser, as it shows that the flow rate (and by extension the reverse thrust) can be recovered back up to (and in some cases above) the levels provided by the baseline geometry.

The flow mechanisms affected by the fluidic actuation may be inferred from the changes in static pressure distributions on the surface of the bullnose. Figure 12b shows how the flow control lowers the pressure over the bullnose and moves the separation point further downstream. The fluidic oscillating jets inject a large number of small scale structures into the flow near the separation point. The ensuing spanwise formation of streamwise vorticity concentrations along the surface that is adjacent to the flow alters the apparent aerodynamic shape of the surface and thereby the streamwise pressure gradient. This, in concert with the momentum addition, accelerates the boundary layer and forestalls the onset of separation. The accelerated flow attaches to the coanda-like bullnose surface, causing a low pressure region over this curved flow control insert. The low pressure region serves to further vector the flow back toward the surface and in a direction more conducive to efficient flow through the turning vanes. The fact that the flow control is able to exploit these effects is the dominant reason why such a small amount of flow applied to the jets is able to enact such large 'global' changes throughout the duct, as reflected in the changes in mass flow rate (Figure 12a). The static pressure distribution on the upper surface (Figure 12c) indicates that even though there is a significant increase in mass flow rate through the duct and associated changes in pressure on the surface of the bullnose, the pressures on the opposite surface is virtually unchanged. As previously discussed, additional flow control applied to this surface could potentially provide further reduction in the losses associated with the flow in this area.

The corresponding data for the highest surface curvature of the A4 bullnose are shown in Figures 13a and b. Unlike the bullnose A2, the small physical dimensions of A4 prevented the co-location of static pressure ports with the fluidic actuators, resulting in a gap in the pressure profiles. Despite the sparse pressure ports, the changes in the slope of the pressure profile downstream from the minimum pressure area ($x/H > 0.25$) upon actuation (Figure 13a) indicate that the flow is nominally attached when the flow control is activated. Furthermore, the fact that the slope is monotonically increasing up to the end of the bullnose should indicate

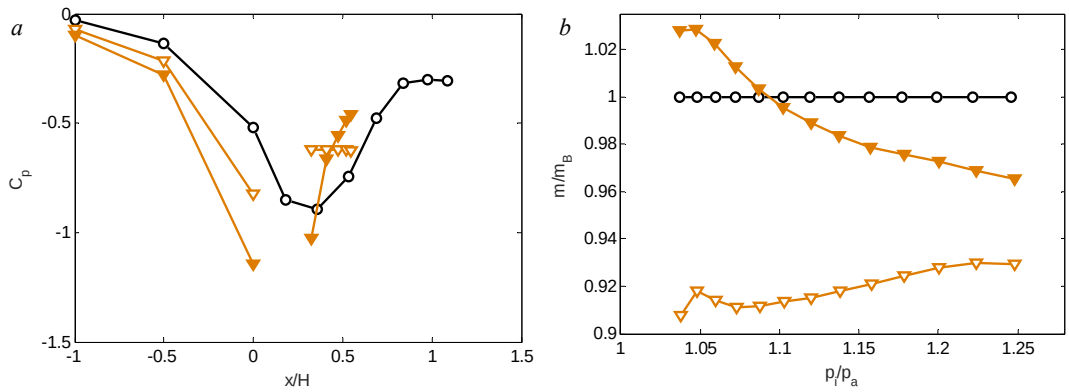

Figure 13. *a) Streamwise variation of the static pressure on A4 (L/H = 0.8) at p_i/p_a = 1.25 in the absence (▽) and presence (▼) of actuation, C_q = 1.3%; the pressure distribution over B (L/H = 1.7) is included for reference (○), and b) Variation of the mass flow rate recovery with p_i/p_a*

that the flow also remains fully reattached, even with the larger streamwise pressure gradient associated with the higher curvature of the A4 bullnose.

The effect of the flow control on the flow rate through the facility for the A4 bullnose is shown in Figure 13b. With the flow control active, the mass flow rate through the thrust reverser is increased across the pressure range tested. However, while the flow appears fully attached, the mass flow rate is not recovered to the same extent as was seen in Figure 12a for the longer A2 bullnose. For example, at higher pressure ratios (p_i/p_a = 1.24), the A2 bullnose was able to recover to $\dot{m}/\dot{m}_B$ = 0.995 (Figure 12a), whereas for the same pressure ratio (and mass flow rate supplied to the jets), the A4 bullnose recovers to $\dot{m}/\dot{m}_B$ = 0.965 (Figure 13b). This is due in part to the larger adverse pressure gradient imposed by the sharper curvature of the A4 bullnose (cf. Figure 9a). In addition, it is postulated that the cascade array is not optimized for the flow vectoring that is generated by the attachment of the flow over the A4 bullnose. The flow attachment over the A4 bullnose causes a vectoring of the flow angle that is steeper than what would be generated by attachment over the baseline B bullnose. As there is no change in the cascade array orientation to account for this steeper angle in oncoming flow, this is one potential cause of losses in the controlled flow. Furthermore, oil-flow visualization experiments (not shown for brevity) indicate that the spanwise nonuniform separation (originally pointed out in Figure 8 for the baseline bullnose) becomes exacerbated with increasing adverse pressure gradient. Although it should be possible to approach the baseline bullnose performance by increasing the mass flow rate to the jets (i.e., C_q) in the most aggressive A4 geometry, it was decided not to exceed C_q of 1.3% due to consideration of potential scale-up and full system integration.

The performance of flow control installed on the most aggressive geometry, A4, is shown in Figure 14 in terms of $\dot{m}/\dot{m}_B$ for a range of pressure ratios. The data in the absence of actuation are shown for reference, already seen in Figure 9. The recovery of the flow through the facility upon activation of the jets at high pressure ratios (p_i/p_a = 1.25) results in an increase in the flow rate through the facility of 2.5%. At low flow rates (p_i/p_a = 1.06), the flow rate through the facility is recovered to levels 3% higher than the baseline. All the data in Figure 14 corresponding to constant mass flow rate to the jet array exhibit a decrease in recovery of mass flow rate through the facility for increasing pressure ratio, which is a direct consequence of reduced C_q. The linear offset with increased actuation strength indicates that the flow control array has yet to 'saturate' and that further increases in mass flow provided to the jet array would generate similar increases in mass flow rate through the facility. Small increases in flow rate to the jet array continue to further effect the global flow field in a manner that decreases losses through the duct for increasing actuation levels. The vertical offset in the curves with increased mass fraction supplied to the flow control array indicates the recovery as a function of mass flow rate to the jets ($\dot{m}_j$) and the pressure ratio, which is further examined in Figure 14b.

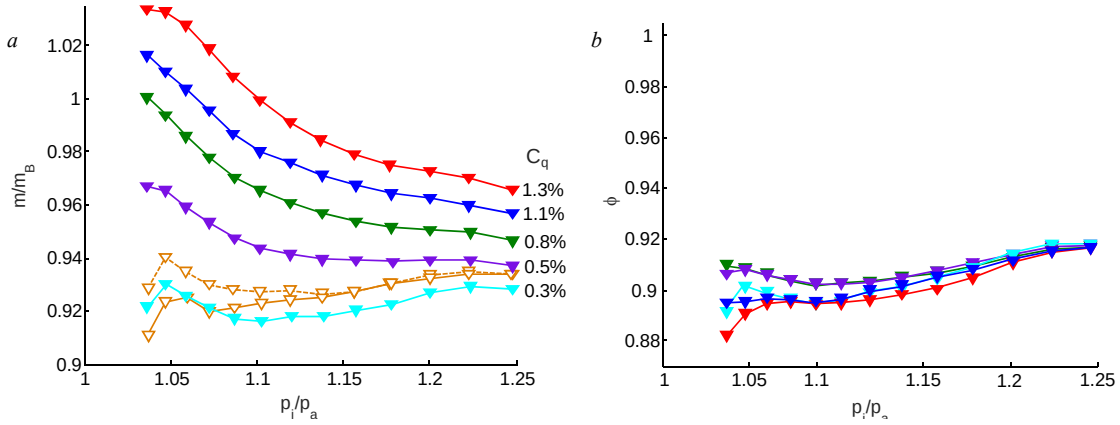

Figure 14. *Mass flow rate recovery (a) and the reduced recovery parameter (b) distribution with p_i/p_a for the A4 configuration (L/H = 0.8) and the flow control parameter range C_q = 0 – 1.3%. Baseline flow over a smooth A4 moldline is shown for reference in dashed line.*

The mass flow rate to the jets ($\dot{m}_j$) is found to be directly proportional to the offset in the curves shown in Figure 14a and exponentially related to the pressure ratio by the function $\phi = (\dot{m}/\dot{m}_B) - \kappa\dot{m}_j(p_i/p_a)^{-6}$. The constant κ is used to non-dimensionalize $\dot{m}_j$ and to linearly scale the offset parameters. The two terms on the right-hand side represent the mass flow rate recovery (relative to the baseline bullnose B) and the lump nonlinear effect of the flow control and the pressure ratio, and this functional form is based on the trends observed in Figure 14a, as an empirical relationship. Figure 14b indicates that the scaling function collapses all the controlled cases onto the unified dependence on the pressure ratio, especially at the higher levels of p_i/p_a. This indicates that at any p_i/p_a = *const*, mass flow rate recovery is linearly proportional to the mass flow rate through the control jets. Inversely, if the flow control rate through the jets is kept constant, the mass flow rate recovery would sharply decay with p_i/p_a due to its $(p_i/p_a)^{-6}$ dependence. In general, the functional relationship shown in Figure 14b enables an estimate of the mass flow rate recovery for any given flow condition (pressure ratio) and the flow control mass flow rate, within the tested domain.

Details of the flow over the A2 bullnose in the presence of jet actuation are further investigated using fog visualization. For this purpose, fog is introduced at the inlet to the facility and it seeds the entire volume of the bullnose upstream flow. The investigated domain (Figure 15a) extends from the jet actuator array upstream that is visible on the bullnose surface in Figures 15b and c. Note that section of the bullnose surface and its cascade also become visible in the background due to internal reflections of the incident planar laser sheet used for illumination. In the absence of actuation (Figure 15b), the visualization images show a domain of flow separation that is marked by the low concentration of fog particles, as the separated flow is sparsely seeded due to indirect entrainment of the fog particles through the shear layer. When the actuation is applied (Figure 15c), the flow appears completely attached to the surface of the bullnose, as indicated by the presence of full-seeded flow near the surface.

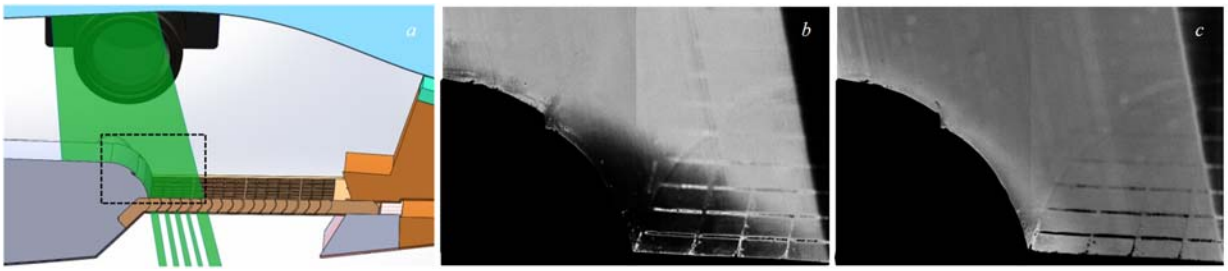

Figure 15. *Seeded-flow visualization of the flow separation over the A2 (L/H = 1.4) bullnose in the absence (b) and presence, C_q = 1.2% (c) of actuation. Visualized field of view is schematically shown in (a).*

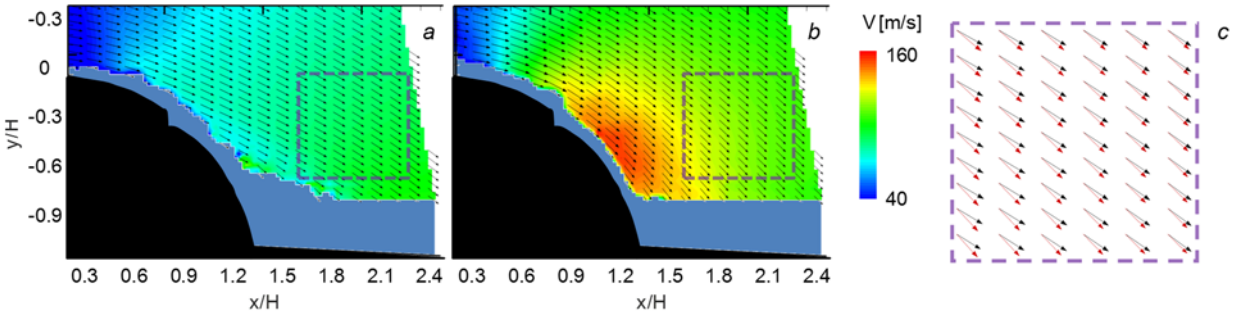

Figure 16. *PIV measurements in the cross stream (x-y) plane over the A2 (L/H = 1.4) bullnose: Color raster plots of the velocity magnitude superposed with velocity vectors in the absence (a) and presence, C_q = 1.2% (b) of actuation. Extent of the flow vectoring is emphasized over a zoomed-in field (c) showing uncontrolled (black) and controlled (red) mean velocity vectors.*

The changes in the flow field induced by the actuation jets are measured using particle mage velocimetry (PIV). Figure 16a and b show color raster plots of velocity magnitude that are superposed to velocity vectors in the *x-y* plane along the centerline of the duct in the domain of $0 < x < 2H$, $-1H < y < 0.37H$. Due to surface reflections, it was not possible to resolve vectors near the surface (masked in blue). Comparison of Figure 16a and b indicates that the actuation leads to an increase in the flow speed by as much as 100% within the region in the vicinity of the bullnose. The spreading of the effect of the jets is due in part to the Coanda effect. The jets issue as near wall jets due to their proximity to the curved surface. As the flow leaves the orifice, it moves along the surface at high speed and generates a low pressure region, which vectors the duct flow toward the surface of the bullnose. This, combined with the resulting curvature of the streamlines, results in a region of high speed, which influences a large portion of the flow within the duct. The vectoring of the flow is also emphasized in Figure 16c for a sub-domain of the flow measurements. Comparison of the direction of the vectors indicates the flow is significantly vectored toward the cascades, especially in the region near the bullnose. This effect diminishes with distance away from the actuators, but the flow remains notably vectored even at a distance *H* away from the actuators. Such changes in direction and magnitude of the velocity in this region have a global effect on the flow, as has been indicated by the increase in mass flow rate through the facility upon flow control activation.

Former analysis is primarily focused on the mass flow rate through the reverser duct, as an indirect indicator of improvements in the related thrust that such a duct would generate. In order to further examine the flow control effect on the generated thrust, the magnitude and direction of the flow exiting the duct through the cascades is examined with the A2 bullnose geometry. The flow exiting the thrust reverser test section through the cascades is measured using PIV and is shown in Figure 17 using color raster plots of the velocity magnitude in the *x-y* plane superposed with velocity vectors in the absence (Figure 17a) and presence (Figure 17b) of actuation. The field of view is directly downstream of the cascades, and the yellow marks along the top surface indicate the location of the turning vanes within the cascades. The yellow line in the top left-hand corner of the image shows the outer surface of the bullnose in the present view. In the absence of actuation, there is a domain of low-speed flow near the outer surface of the

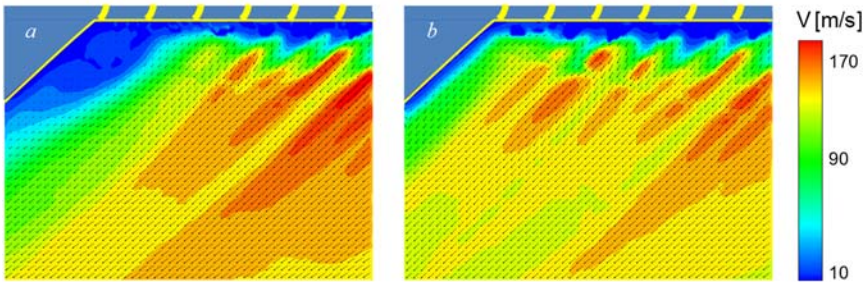

Figure 17. *Color raster plots of velocity magnitude superposed with velocity vectors in the cross stream x-y exit plane of the thrust reverser in the absence (a) and presence, C_q = 1.2% (b) of actuation over A2 (L/H = 1.4) bullnose. The cascade vanes are false-colored in yellow along the top surface.*

bullnose downstream of the cascade (Figure 17a) that is the result of the separated flow on the surface of the bullnose upstream of the cascade (cf. Figure 15). The separation on the bullnose substantially decreases the flow through the first two vanes (closest to the bullnose). Farther to the right, the flow downstream of the vanes is characterized by streaks of high-magnitude velocity through the gaps between the vanes that are interlaced with lower velocity streaks that correspond to the wakes of the vanes. When the actuation is applied (Figure 17b), the extent of the separation is significantly diminished, there is a significant flow through the first two vanes, and the flow field is turned towards the bullnose. The reduced blockage associated with the collapse of the separated flow leads to a decrease in losses and an increase in the mass flow rate through the thrust reverser.

The effects of the actuation at C_q = 1.3% (relative to the baseline bullnose configuration B with a pressure ratio of p_i/p_a = 1.25) on $\dot{m}/\dot{m}_B$ for a range of pressure ratios and bullnose geometries (B-A4) is depicted in Figure 18. In the presence of actuation, the performance of B and A1 is nearly identical, indicating that the actuation is sufficient to overcome the change in geometry of A1, and that the baseline geometry location of the jets is not optimal for the baseline geometry as it is for the A1 geometry. There is also a distinct fall off in jet performance which follows both the pressure ratio increase and the decrease in bullnose length, with B and A1 being exceptions. Furthermore, the A4 geometry performs better at the lowest pressure ratios tested p_i/p_a = 1.04. At these low pressure ratios, the jets are able to impart a larger vectoring of the flow. Due to this effect, the flow over the rest of the cascade is less disturbed by the previously separated flow over the bullnose, improving the flow through the entire facility. Further examination of the trends, both with pressure ratio and with bullnose length, is shown in Figure 18b.

As was the case with Figures 11 and 14, scaling factors are applied in order to examine trends in the data. The active flow control cases are scaled by the factors that were determined to be functions of both pressure ratio (p_i/p_a) and bullnose length (L). The scaling parameter also includes the mass flow rate to the jets ($\dot{m}_J$), but it is a constant for all the tested cases. These two scaling laws, first introduced in the discussion of Figure 11 and 14, are combined, resulting in function $\gamma = \left[(\dot{m}/\dot{m}_B) - \kappa \dot{m}_j (p_i/p_a)^{1.8(L_B/L)^{1.6}}\right](L_B/L)^{0.1}$. Note that the functional dependence on the pressure ratio (p_i/p_a) is different for each bullnose. The non-linearity in the functional relationships shown in Figure 18a becomes more apparent for bullnoses that have higher curvature, due to the fact that the separation domain forms at lower pressure ratios and becomes larger (and generates more losses) at lower pressure ratios. For this reason, the more aggressive bullnose behavior, as a function of pressure ratio, exhibits itself as a non-linearity when scaled by the mass flow rate through the facility. The exponential parameter which scales the (p_i/p_a) was found to have a functional dependence on the bullnose length. The scaling constant κ, which is used to non-dimensionalize the mass flow rate and to provide a fit parameter, is the same for all of the curves presented *except* for A1 where it was multiplied by 1/65 to get the curve fit that is presented in Figure 18b. The behavior of the A4 geometry

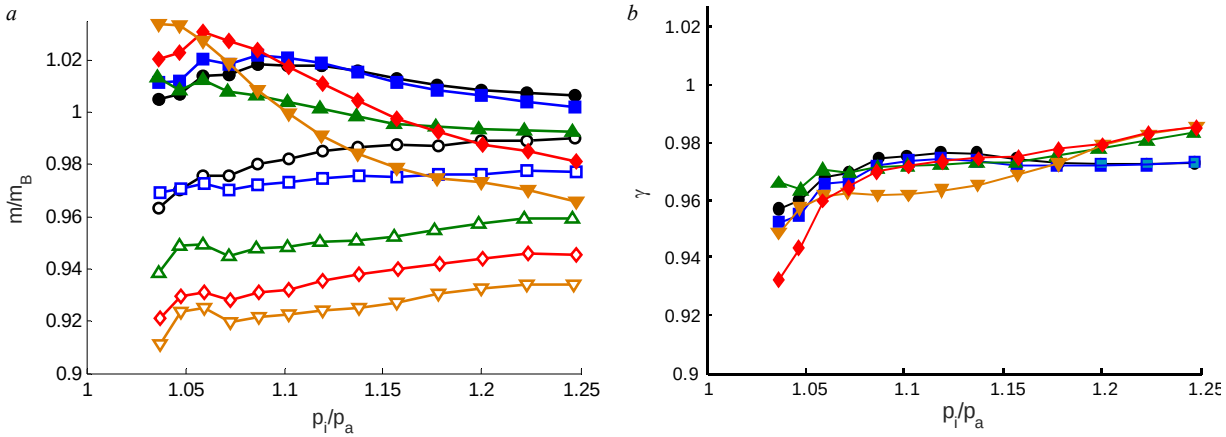

Figure 18. *Mass flow rate recovery (a) and the reduced mass flow rate (b) variations with pressure ratio p_i/p_a for the bullnose configurations L/H = 1.7 (○), 1.4 (□), 1.1(Δ), 1.0 (◊), 0.8 (▽).*

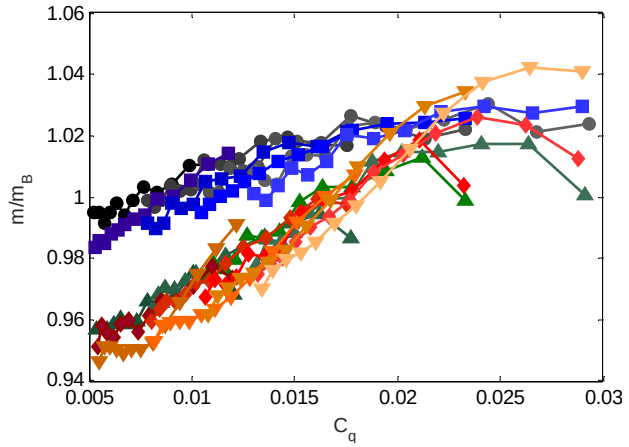

Figure 19. *The mass flow rate recovery with the flow control mass flow rate coefficient for the bullnose geometries L/H = 1.7 (●), 1.4 (■), 1.1(▲), 1.0 (♦), and 0.8 (▼).*

bullnose departs from the behavior of the others tested for the range of $1.06 < p_i/p_a < 1.16$. It is postulated that this departure is due to the high curvature of the A4 bullnose which, when used to vector the flow, provides non-optimal flow to the first row of cascade array. However, this is in contrast with the higher pressure ratios ($p_i/p_a >$ 1.18.), where the B and A1 bullnose provide almost identical performance, and A2, A3 and A4 all scale in a similar fashion. The differences in behavior between B and A1 and the rest of the bullnoses indicate that there is a significant difference in the way which flow control is affecting the flow in these two geometries. It is argued that these differences are due in part to the ability of these two geometries (B and A1) to provide almost ideal flow (vector angle) for the cascades nearest to the bullnose, as with more aggressive bullnoses this increased vectoring provides increased losses through the first cascade by 'over vectoring' the flow. This distinction between B and A1 and A2-A4 is further examined in Figure 19.

The families of bullnose shapes with active flow control at various levels are examined as a function of mass fraction to the jets ($\dot{m}_j/\dot{m}$). Examination of Figure 19 shows that A2, A3 and A4 all collapse down to a single curve, indicating that there is a strong linear dependence between the mass fraction supplied to the jets and the resulting improvement in mass flow rate through the facility. This trend is independent of geometry for the three most aggressive geometries. The fact that the flow rate through the facility is a stronger function of the mass fraction than it is of the geometry is very important to the design of the flow control installation. For example, if the mass flow rate supplied to the jets is a critical design constraint, it is possible to select the geometry which would provide the acceptable level of performance directly from this relationship. The exception is the difference between the B and the A1 geometries and the more aggressive geometries (A2-A4). These different trends are due to the fact that the lower pressure gradient (due to the larger radius of curvature) allows for the flow to be reattached at lower supply rates to the flow control jets. As the mass fraction increases, the flow is attached over a greater portion of the bullnose, which is why, at higher mass fractions ($\dot{m}_j/\dot{m} > 0.02$), the geometries behave in a similar fashion whereas, at lower mass fractions, the flow is dominated by the separation inherent to the more aggressive geometries. Bullnose geometries more aggressive than the A1 geometry affect the flow rate throughout the duct in a stepwise, non-linear fashion, which indicates that there is some sort of 'tipping point' reached that merits further investigation. In general, Figure 19 illustrates that a particular mass fraction is needed in order to affect the flow through the duct in the same way and that this trend is almost independent of geometry. Furthermore, while the B and A1 geometries 'saturate' at around $\dot{m}/\dot{m}_B = 1.03$, the A4 geometry, for the same mass flow rate supplied to the active flow control, is able to achieve mass flow ratio of $\dot{m}/\dot{m}_B =$ 1.04. This is another indication that, for higher mass fractions to the active flow control, the more aggressive geometries with active flow control have the potential to perform better than the baseline geometry.

5. Conclusions

In the thrust reverser duct, potentially beneficial reduction in the streamwise length of the internal flow turning surface (a bullnose) is limited by the engendered flow separation and the ensuing losses. The present experimental investigations explored effectiveness of the active flow control in mitigation of detrimental effects of the bullnose shortening over a range of pressure ratios p_i/p_a = 1.04 – 1.25 (i.e., $M \approx$ 0.24 – 0.53). The model section of the cascade thrust reverser was an annular sector of 55° that accommodated five bullnose geometries of a given height H and decreasing length: L/H = 1.7, 1.4, 1.1, 1.0,

and 0.8. Each bullnose module had the same array of fluidic oscillating jets, integrated at the fixed streamwise location that was based on the respective baseline flow separation line. The flow control parameter was defined as the mass flow rate coefficient C_q, which relates the total mass flow rate to the control jets to the thrust reverser mass flow rate for the nominal baseline bullnose (L/H = 1.7).

The main indicator of the flow control effectiveness was a percentage of the mass flow recovery in the thrust reverser relative to the baseline bullnose (L/H = 1.7). It was shown that the mass flow rate recovery for a given bullnose geometry and the flow condition (i.e., pressure ratio) is directly proportional to the mass flow rate of the control jets. Alternatively, the mass flow rate recovery for a given geometry and the jets mass flow rate decreases in a nonlinear fashion. Given the upper limit to the flow control mass flow rate, the flow control effectiveness therefore decreases with an increase in the pressure ratio. However, it was demonstrated that the flow control was capable of not only recovering, but even exceeding the duct mass flow rate for the reduced bullnose length by 18% (compared to the same flow conditions for the baseline bullnose) , and most of the range of p_i/p_a. The peak effectiveness decreases with a reduction in the bullnose length, such that an increase in the thrust reverser mass flow rate between 2.5 – 3% upon the flow control in the bullnose shortened most aggressively by 53%.

The scaling laws were developed that relate the mass flow rate recovery, the flow control mass flow rate, flow conditions (pressure ratio), and the flow geometry (bullnose length) for the full space of the explored parameters. Finally, dependence of the mass flow rate recovery on the relative flow control mass flow rate, for all of tested cases, indicated two dominant flow control trends split between the low- and high-curvature bullnose geometry. The former, comprised of L/H = 1.7 and 1.4, is characterized by high receptiveness to even the lowest levels of the flow control C_q and saturation of the mass flow rate recovery at about C_q = 1.7%. It should be noted that the saturation level generates mass flow rate through the thrust reverser that even exceeds the levels of the nominal, full-length bullnose. In the case of the high-curvature, aggressive bullnoses (L/H = 1.1, 1.0, and 0.8), the mass flow recovery is offset to lower levels, but it increases at higher rate with C_q, such that it eventually even exceeds the saturation levels of the low-curvature geometries, only at higher C_qs.

The present study demonstrated that the performance decrement due to reductions in the overall length of the thrust reverser can be overcome using an active flow control approach that utilizes a spanwise array of fluidic oscillating jets. These results indicate that systems level benefits are possible though the use of flow control applied to a thrust reverser of reduced length.

Acknowledgements

This work was supported by the Boeing Company.

References

Arbiter, D. G., “An investigation at static conditions of nonaxisymmetric nozzle thrust reverser port geometry including effects of rounding and rotating the port corner,” *NASA Report* NASA-CR-178036, 1985.

Butterfield, J., Yao, H., Curran, R., Price, M., Armstrong, C., and Raghunathan, S., “Integrated Methods for the Design of a Thrust Reverser Cascade,” *Journal of Propulsion and Power*, July 2006, pp. 826-871.

Dietrich, D.A. and Gutierrez, O.A., “Performance of a Cascade Thrust Reverser for Short-Haul Applications,” *Journal of Aircraft*, Vol. 13, 1976, pp. 185-191.

Gregory, J.W. and Tomac, M.N., “A Review of Fluidic Oscillator Development and Application for Flow Control,” *AIAA Paper* AIAA-2013-2474, 2013.

Hall, S., Cooper, R, and Raghunathan, S, “Fluidic Flow Control of a Natural Blockage Thrust Reverser,” *AIAA Paper* AIAA-2006-3513, 2006.

Hegen, G.H. and Kooi, J.W. “Investigation of Aircraft Performance with Deployed Thrust Reversers in DNW,” *AIAA Paper* AIAA-2005-3702, 2005.

Ho, C-M. and Huerre, P., “Perturbed Free Shear Layers”, Ann. Rev. Fluid Mech., Vol. 16, 1984, pp. 365-424.

Johns, C. J., “Solution of an engine inlet compatibility problem during C-17 low cost N/EAT nacelle thrust reverser development,” *AIAA Paper* AIAA-2000-5579, 2000.

Kohl, R. C. and Algranti, J.S., “Investigation of a Full-Scale, Cascade-Type Thrust Reverser,” NACA TN # 3975, 1957.

Poland, D.T., “The Aerodynamics of Thrust Reversers for High Bypass Turbofans,” *AIAA Paper* AIAA-67-418, 1967.

Raghu, S., “Fluidic oscillators for flow control”, Experiments in Fluids, Vol. 54, 2013, pp.1-11.

Smith, T.E., “Gas turbine engine power plants for aircraft”, US Patent #4,047,381, 1977.

Vukasinovic, B., Rusak, Z. and Glezer, A., “Dissipative small-scale actuation of a turbulent shear layer”, Journal of Fluid Mechanics, Vol. 656, 2010, pp. 51-81.

Wood, S. K. and McCoy, J., “Design and Control of the 747 Exhaust Reverser Systems,” SAE Paper 690409, 1969.

Yetter, J.A., “Why do Airlines Want and Use Thrust Reversers?” *NASA Report* NASA-TM-109158, 1995.